

In situ observation of void evolution in 1,3,5-triamino-2,4,6-trinitrobenzene under compression by synchrotron radiation X-ray nano-computed tomography

Liang Chen,^a Lihui Wu,^a Yu Liu^{b*} and Wei Chen^{a*}

Received 26 April 2019

Accepted 21 October 2019

Edited by S. Svensson, Uppsala University, Sweden

Keywords: X-ray nano-CT; three-dimensional imaging; 1,3,5-triamino-2,4,6-trinitrobenzene (TATB); void formation and development; crack formation and development; compressive loading.

Supporting information: this article has supporting information at journals.iucr.org/s

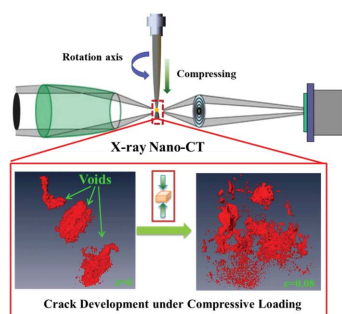
^aNational Synchrotron Radiation Anhui Provincial Engineering Laboratory of Advanced Functional Polymer Film, CAS Key Laboratory of Soft Matter Chemistry, University of Science and Technology of China, Hefei, Anhui 230029, People's Republic of China, and ^bInstitute of Chemical Materials, China Academy of Engineering Physics, Mianyang, Sichuan 621900, People's Republic of China. *Correspondence e-mail: liuyu307@caep.cn, wc003@ustc.edu.cn

The formation and development of voids in 1,3,5-triamino-2,4,6-trinitrobenzene crystals under compression were characterized *in situ* by X-ray nano-computed tomography. Benefiting from high spatial resolution (30 nm) and excellent imaging contrast, the X-ray nano-computed tomography images revealed the presence of a small fraction of inhomogeneous structures in the original crystal (volume ratio $\sim 1.2\%$). Such an inhomogeneity acts as a nucleation of voids and produces stress concentration during compression, which leads to continuous growth of the voids under loading. Meanwhile, the results further reveal that the developing voids are not isotropic: voids with higher surface roughness and irregular structures are easier to break and form new micro-voids. These new voids with higher irregular structures are weaker and easier to break into smaller ones compared with the originals, leading to the development of voids along these weak zones. Finally large voids form. The experiments allow direct investigation of void formation and development, which helps in studying the mechanisms of void development and energetic materials deterioration during manufacturing and transporting.

1. Introduction

1,3,5-Triamino-2,4,6-trinitrobenzene (TATB) with polymer-bonded explosive (PBX) is widely used in defense and commercial business due to its excellent performance such as its high explosiveness and safety properties (Parab *et al.*, 2016; Dienes *et al.*, 2006; Barua *et al.*, 2012; Chen *et al.*, 2007). Under real conditions, *i.e.* during manufacturing, storing and transporting, PBX can be subjected to various dynamic loadings, which could cause the formation of micro-voids and to other damage, and lead to the decrement of its mechanical and safety properties (Yeager *et al.*, 2012; Ricard *et al.*, 2014; Balzer *et al.*, 2004). Such macroscopic performance is closely related to the micro-structure evolution of PBX. Therefore, studying the response of PBX under dynamic loadings is important for unveiling damage mechanisms, and valuable for manufacturing and maintaining good performance.

One of the important factors weakening PBX under dynamic loadings is the formation and development of voids. Besides the de-bonding between the TATB crystals and polymer binder (Yuan *et al.*, 2018), flaws in TATB developing under dynamic loadings are also an important factor in the formation and development of voids (Xue *et al.*, 2010; Gallagher *et al.*, 2014; Chen *et al.*, 2005, 2007; Siviour *et al.*, 2008). The formation and development of voids is complex, and



several factors need to be considered, including void nucleation and the growth of short voids which then develop into macroscopic voids (Yuan *et al.*, 2018). Moreover, the initial voids have certain geometrical shapes, which could contribute to the anisotropic growth of the voids. Unveiling the fundamental mechanism of the evolution of the voids requires obtaining structural information of the voids with high spatial resolution and excellent imaging contrast. Therefore, tracking the fine structural evolutions of voids during dynamic loading is important for understanding the damage mechanisms and deterioration of TATB (Wu *et al.*, 2012; Zhou *et al.*, 2012; Peterson *et al.*, 2001).

The key to studying the evolution of the voids is selecting proper imaging techniques to capture *in situ* their structures during dynamic loading, especially three-dimensional (3D) structures. After decades of investigation, several techniques have been used to capture the voids of crystals (Chen *et al.*, 2017; Cui *et al.*, 2019; Cheng *et al.*, 2007; Rae *et al.*, 2002; Yuan *et al.*, 2018), such as visible-light microscopy, scanning electron microscopy and atomic force microscopy, which provide new insights for studying void morphologies and characteristics. However, because of the particular characteristics of these techniques, results have mainly concerned the surface properties of voids or large voids and it is difficult to obtain the particular morphologies of certain voids. Hard X-ray micro-computed tomography (X-ray μ -CT) has the capability of capturing void morphologies and has been proven to be an effective characterization technique (Wu *et al.*, 2017; Garcea *et al.*, 2014, 2015). However, hard X-ray μ -CT with energies of several tens of kilo-electronvolts has high penetrating abilities but poor imaging contrast for light elements such as C, N, H and O (the main constituting elements of TATB). Moreover, hard X-ray μ -CT always has relatively low spatial resolutions (several hundred nanometres) (Wu *et al.*, 2017). These all make it difficult to view the fine structures of the voids, such as their sharp tips and surface roughness, and only large voids can be well distinguished. With the fast development at low energies of soft X-ray nano-computed tomography (nano-CT) (X-ray energy \simeq several hundred eV), its distinguished characteristics, such as high spatial resolution (~ 30 nm) and high imaging contrast, make it suitable for studying micro-void formation and development on the nanometre scale (Sorrentino *et al.*, 2015; Le Gros *et al.*, 2014; Jian *et al.*, 2016). Additionally, soft X-rays can interact strongly with light elements such as C, H, O and N. Micro-voids causing a density decrease in local regions will lead to excellent imaging contrast, and it is possible to precisely distinguish the morphologies and geometries of micro-voids and their development as well as nucleation and the original short voids under dynamic loading.

In this study, aiming to investigate *in situ* the formation and development of voids under loading, TATB crystals were imaged by X-ray nano-CT using a custom-built micro-compressive device. The 3D structure and the evolution of voids under dynamic loading were captured and quantitatively analyzed. The results show that there are micro-voids in the original crystal which act as nucleation sites and later develop into large voids under continuous compression. The growth of

voids finally leads to the destruction of the TATB crystal, crushing into smaller pieces. The experiments provide new insights into the evolution of voids within the TATB crystal with high spatial resolution and excellent imaging contrast. Such a technique can be further extended to other systems, such as metal fatigue under dynamic loading.

2. Materials and characterization techniques

2.1. Materials

The TATB crystals were kindly provided by the China Academy of Engineering Physics with size distribution from $5\ \mu\text{m}$ to $50\ \mu\text{m}$ and used as received. A crystal was first adhered to the top of a pin and then installed in the homemade compressive device with a micrometre screw to compress the samples (adjusting precision: $0.5\ \mu\text{m}$). Crystal adhering and compression were performed using an inverted microscope, as shown in Figs. 1(a) and 1(b). The original crystal was first imaged by X-ray nano-CT at tilting angles ranging from -70° to 70° with an interval of 0.5° . Afterwards, the crystal was compressed to predetermined distances using the micrometre screw. The distance moved (Δl) to compress the crystal was $1\ \mu\text{m}$ each time, and then the loading strains were calculated as $\varepsilon = \Delta l/l_0$ (where l_0 is the original height of the crystal). Then the crystal was imaged again using the same tilting angles.

2.2. X-ray nano-CT

In the experiment, two X-ray nano-CT systems were used for 3D imaging under compression. One was soft X-ray nano-CT on beamline BL07W at National Synchrotron Radiation Laboratory (NSRL; X-ray energy: 520 eV, spatial resolution:

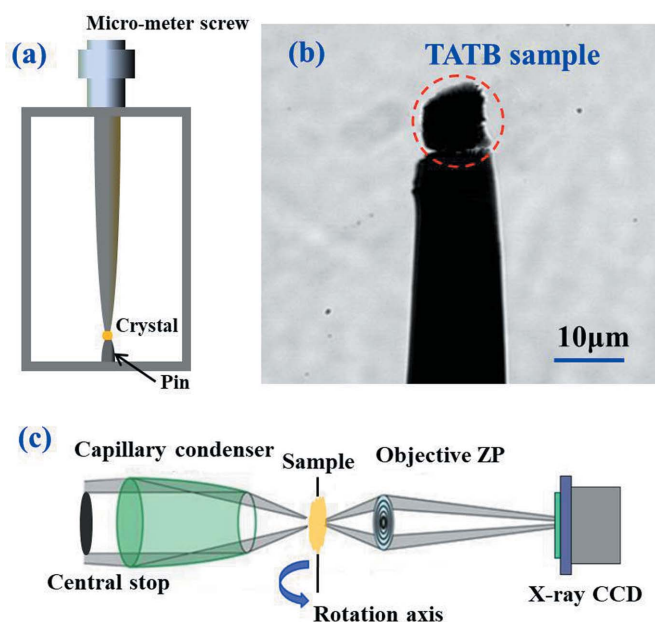


Figure 1
(a) Schematic of the homemade compressive device. (b) Visible-light microscope image of the crystal adhered on top of the pin. (c) Schematic of the optical setup for soft X-ray nano-CT.

30 nm), and the other was hard X-ray nano-CT on beamline 4W1A at Beijing Synchrotron Radiation Facility (BSRF; X-ray energy: 8 keV, spatial resolution: 100 nm) (Yuan *et al.*, 2012). Briefly, synchrotron radiation from a wiggler was first monochromated and then focused by an elliptical capillary condenser. Using a zone plate (ZP) as an optical lens, the 2D projections containing sample structural information with different tilting angles were connected by X-ray CCD. Soft X-ray nano-CT was used to study the nucleation and origin of voids and their formation from short voids, with excellent imaging contrast and high spatial resolution. A schematic illustration of the optical setup for X-ray nano-CT is shown in Fig. 1(c). Hard X-ray nano-CT was selected mainly because the sample stage of the system has a large free space for installing the homemade compressive device (Toda *et al.*, 2008; Chen *et al.*, 2015, 2016; Shirai *et al.*, 2014). The crystal can be kept under compression during imaging, which is helpful for following the development of the voids *in situ* under compression. A series of 2D projections of the crystals under different strains were obtained and underwent subsequent 3D reconstruction, segmentation and quantitative analysis.

3. Results and discussion

Fig. 2 shows the 3D reconstruction results of TATB crystals with different morphologies by soft X-ray nano-CT (X-ray energy: 520 eV). Two different types of crystals are shown, namely a single crystal [Fig. 2(a)] and aggregations of crystals [Fig. 2(b)]. 3D reconstruction movies are provided in the supporting information. The results reveal more clearly the

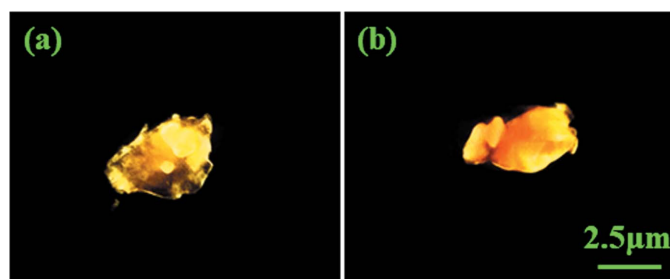


Figure 2
3D reconstruction imagings of (a) a TATB single crystal and (b) an aggregation of TATB crystals by soft X-ray nano-CT.

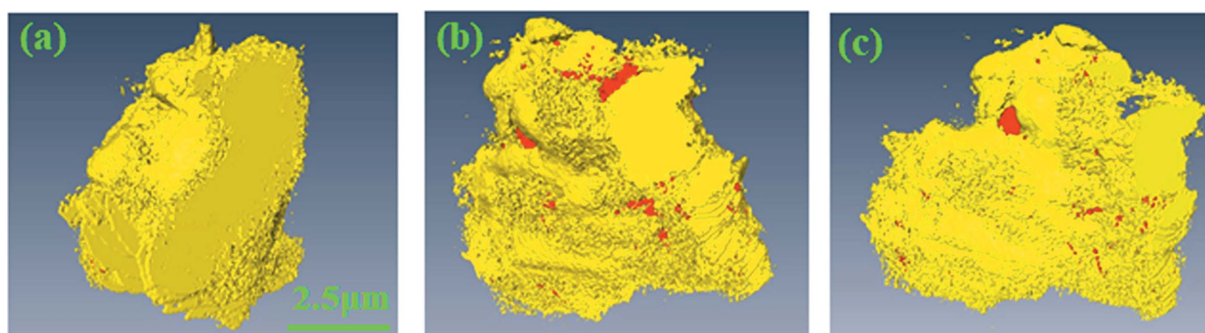


Figure 3
Segmented and dyed results for the TATB crystal under different compressive strains: (a) original crystal; and under a strain of (b) 0.05 and (c) 0.08.

inhomogeneous structures at the micrometre scale as shown by the high- and low-density zones within one crystal. Quantitative analysis of 3D reconstruction imaging is accomplished using *Amira* 5.3.1 software, where different structures can be dyed with different colors for better distinction. Afterwards, the characteristics of crystal and voids were quantitatively analyzed.

In order to mimic the stress conditions and their influence on the evolution of voids, the original intact TATB crystal was first imaged and then compressed using the homemade compressive device with the compressive strain set as 0.05 and 0.08. The pin with the TATB crystal was installed on the sample stage of the soft X-ray nano-CT for X-ray 3D imaging. Fig. 3 shows the segmented and dyed results of the TATB crystal for different strains, where the base of the TATB crystal is dyed yellow while the voids with low densities are shown in red. The dyed 3D movies are provided in the supporting information.

Using the imaging software, the voids were extracted and highlighted as shown in Fig. 4. Several void groups exist in the initial crystal and these groups constitute various micro-voids. Also, these voids are arranged in an irregular way with the coexistence of isolated and connected groups. With respect to the general morphologies, some are approximately linear and some are approximately ellipsoidal. On compressing to a strain of 0.05, some voids broke into smaller ones. However, the influence of external compression is different for different voids, with some deforming severely while others remaining almost intact. Meanwhile, these small voids either remain connected or are isolated. From the imaging, voids responding to external stress apparently form zones with many micro-voids. Further increasing the strain to 0.08 leads to continuous breaking of the voids. But the fragile void domains break into smaller ones more severely, and the breaking micro-zones enlarge further, which indicates that the previous severely breaking voids are weaker and more easily break into smaller ones with continuous loading. The results reveal that the voids take two pathways: (i) breaking of the original large voids into micro-voids, and (ii) growth of small voids; these two always coexist during compression.

Meanwhile, with the 3D imaging, the growth of void volume ratios ($D = V_{\text{void}}/V_{\text{crystal}}$, where V_{void} is the total volume of voids in the crystal and V_{crystal} is the volume of the crystal) was

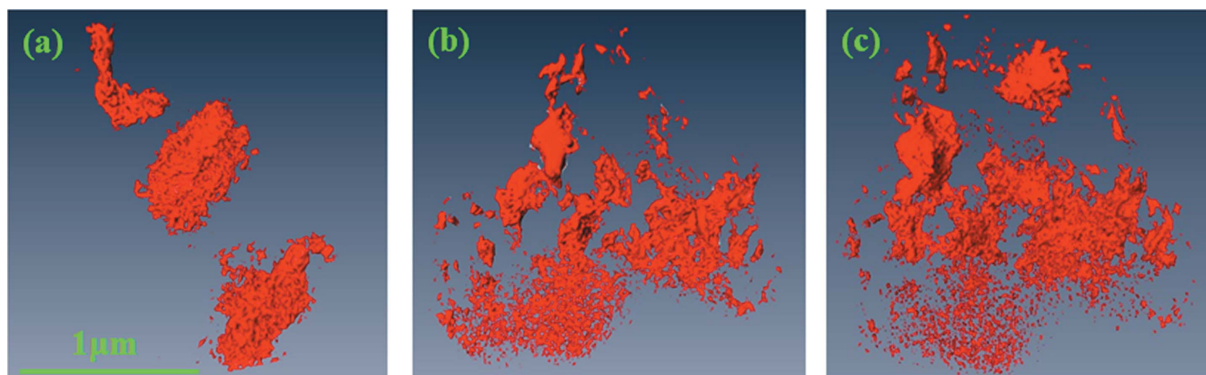


Figure 4
Highlighted morphologies of voids under continuous compression: (a) original crystal, and at strains of (b) 0.05 and (c) 0.08.

calculated to quantify the development of the voids during compression. Fig. 5 shows the void volume ratios D for three different strains. Initially, due to the presence of quite minor defects, the void volume ratio is quite low ($\sim 1.72\%$). Further increasing the strain leads to the increment of D to $\sim 3.11\%$ ($\varepsilon = 0.05$), and finally up to 5.14% ($\varepsilon = 0.08$). This means that the micro-void regions develop during the loading. In order to estimate the structural factors of the voids and their roles in the development of the voids under loading, the fractal dimension {denoted as $d = \lim_{z \rightarrow 0} [\log(N_z)/\log(1/z)]$, where z is the chosen scale, N_z is the volume of the void under the scale z } of the void was used to describe the surface roughness and the self-similar structures of voids at micro-scales. A lower

d indicates a void with higher roughness and irregular structure. The calculated d is also shown in Fig. 5 for comparison. Initially, $d \approx 2.65$, suggesting irregular shapes of the voids of the original crystal. Under compression it decreases to 2.56 , indicating complexity and an increasing of the surface roughness. With continuous compression and large voids breaking into small ones, d decreases to 2.42 . Such results indicate that the new forming micro-voids have higher roughness and irregular structures.

Fig. 4 indicates the non-uniform destruction of voids during compression. In order to precisely analyze the structural factors during void development, the different void groups were extracted. Their individual shapes and the corresponding fractal dimensions were calculated separately and are shown in Fig. 6 and Table 1. The three voids differ in the following ways. For void group I, although its shape is long and thin, its surface roughness is slightly lower than those of the other two, while group III has the highest surface roughness and irregular structures. Group III, where the structures are rougher, is weaker and easier to break into small voids under loading. Under continuous loading, the new forming micro-voids are

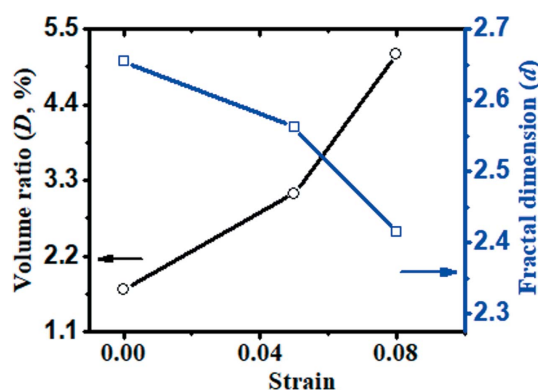


Figure 5
Volume ratio (D) and fractal dimension (d) under compression.

Table 1
Fractal dimensions of the three voids.

	Void I	Void II	Void III
d	2.66	2.62	2.54

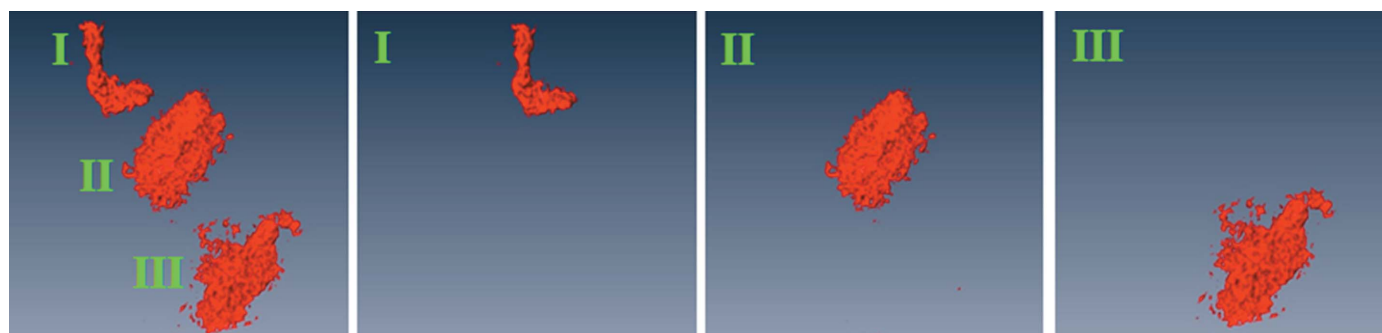


Figure 6
Shapes of three distinct void groups before compression, together with their individual shapes.

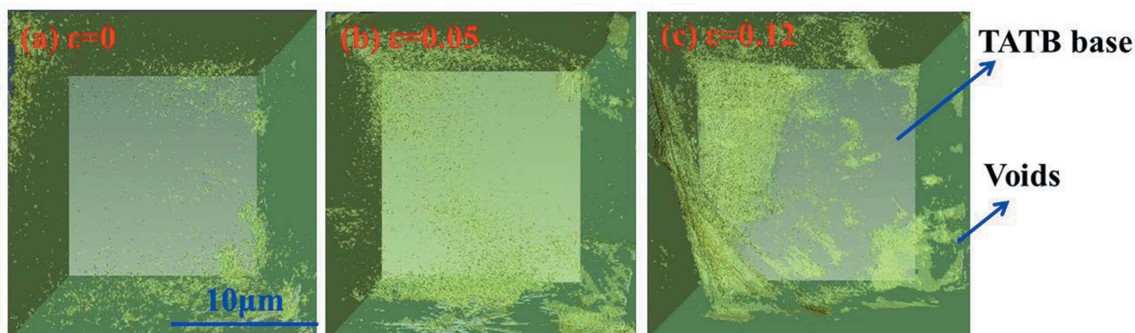


Figure 7 Development of the voids under compression as captured by hard X-ray nano-CT. The TATB base has been made transparent to highlight the void distribution and evolution under compression.

still rough and irregular and are easier to break into smaller ones, which leads to the formation of larger void groups within certain zones and along a specific direction.

The evolution of the voids can be followed by compressing the TATB, keeping the TATB under pressure and imaging the crystal *in situ* in 3D space. Fig. 7 shows 3D imaging of a local region in TATB imaged by hard X-ray nano-CT (X-ray energy: 8 keV); the TATB base is made transparent using software to highlight the void distributions and evolutions in the sample under different compressive strains. Initially some micro-voids are observed and are heterogeneously distributed [Fig. 7(a)]. On compressing to a strain of 0.05 [Fig. 7(b)], an apparent enlargement of the original void groups is observed together with the formation of more micro-voids. Further compressing to a strain of 0.12, with the continuous development of large void groups, the crystal collapses and crushes into smaller pieces.

Meanwhile, the volume ratio (D) and fractal dimension (d) of the voids were calculated and are shown in Fig. 8 to evaluate the void development. Similar to the results obtained by soft X-ray nano-CT, there exist small defects like micro-voids in the original crystal, and $D \simeq 1.19\%$. Under compression, D continuously increases with the development of the voids, and finally reaches 10.17% under a strain of 0.12. This suggests that the breaking voids are easier to break and develop. With further compression, the crystal will crush into small pieces.

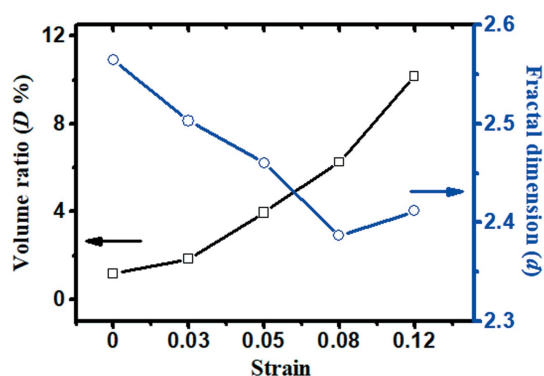


Figure 8 Fracture degree (D) and fractal dimension (d) for different strains.

The fractal dimension of the voids (d), denoting the surface roughness, also suggests that the voids are developing during loading. Initially, $d \simeq 2.57$, which suggests that the micro-voids are not regular and have a certain structure. Compressing to a strain of 0.05, d slightly decreases to ~ 2.46 . This indicates the increment of the roughness of the void. The irregular shapes of the voids may be due to new voids forming as well as short voids growing into long voids. Then d continuously decreases to 2.38 under a strain of ~ 0.08 , which also suggests the formation of more and longer voids. Loading to a strain of ~ 0.12 , it is interesting to see that d slightly increases to 2.51. At this stage, large voids with structures almost throughout form in the crystal. The increase of d means the roughness of the voids decreases and these voids become less irregular.

The voids developing in TATB were followed and their morphologies at different strains were extracted as shown in Figs. 9 and 10, where the TATB is made transparent to highlight the evolution of the voids. The imaging again confirms the presence of void groups in the original crystal. During compression, the micro-void groups start to grow. At the same time, the growth direction of the void is not random but follows certain directions. As described above, the voids first break and develop along zones with relatively more roughness and irregular structures under compression. These new forming micro-void groups are weaker with higher roughness compared with the adjacent zones and are easier to develop

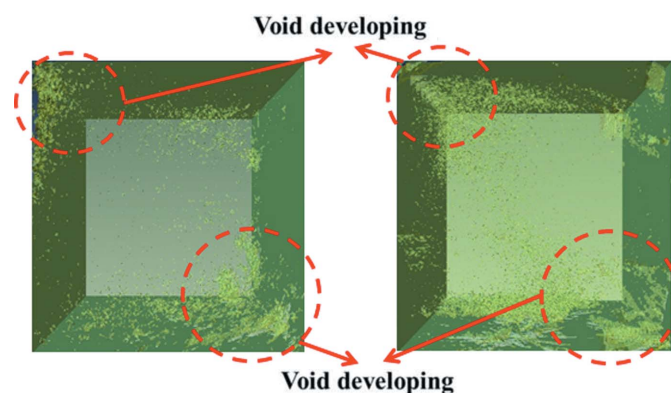


Figure 9 Snapshots of the distribution of voids before and after compression.

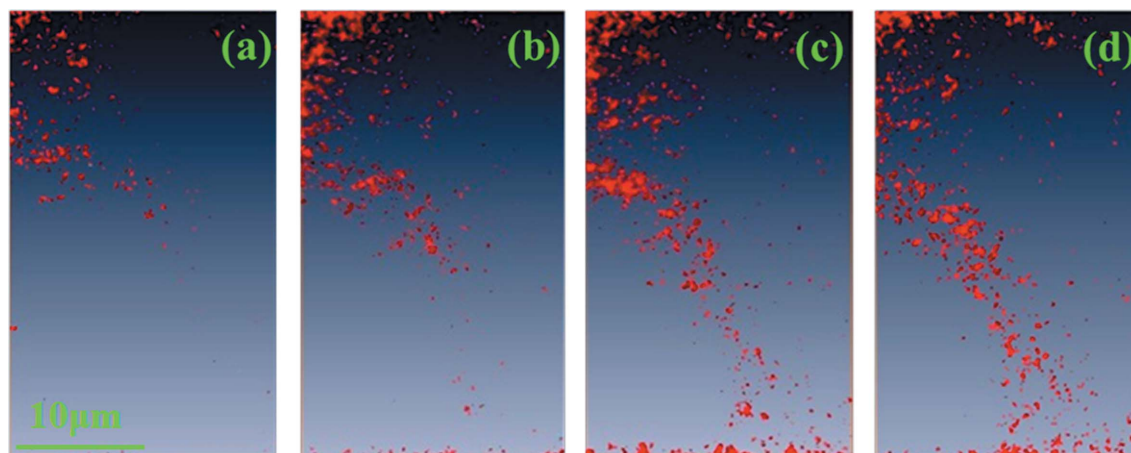


Figure 10
Evolution of voids during compression: (a) original, and under a strain of (b) 0.05, (c) 0.08 and (d) 0.12.

under continuous compression, as shown in Fig. 10(b). Accompanying further compression, the micro-voids develop along the weak region, and finally large voids form until the crystal crushes. The results indicate that, similar to fatigue voids that develop in metal materials that follows group effects under loading (Furuta *et al.*, 2018; Cheong *et al.*, 2009; Landron *et al.*, 2012), the voids developing in the TATB crystal under compression also follow similar effects and form micro-void zones. The void zones continuously develop and finally result in the formation of large voids, which leads to the crystal breaking and reducing performance.

Based on the above results, the evolution of voids in TATB crystals can be generally described as follows: micro-void groups exist in the original crystals, which act as a nucleation site, and such groups continuously grow under compression. Using X-ray nano-CT techniques, the 3D structures of the voids and their development are viewed non-destructively. From the 3D results, as well as the different shapes of the crystals, the inner structures of the crystals are not homogeneous, and high- and low-density zones are coexistent in the crystal. These micro-voids form micro-void zones and can be considered as a nucleation of voids, although its volume ratio is small ($\sim 1.2\%$) compared with the whole crystal. Meanwhile, the further development of different void groups is quite different. Combining with the fractal dimensions, the voids with higher roughness and irregular structures are easier to break into smaller ones and then develop along these directions. We can consider that the irregular and roughness structures produce stress concentration under compression, and these roughness zones bear higher stress compared with adjacent zones and are easier to break. This is coincident with the experimental results that the voids with higher roughness are easier to break and develop during compression. Meanwhile, because the new forming voids have higher roughness and more irregular structures, these new micro-voids bear higher stress and more easily develop into smaller ones with further compression, which leads to an anisotropic development of voids. As a result, based on the morphologies and fractal dimensions of the voids, we conclude that the micro-

voids developing are not isolated but have characteristics of group effects, and experience first the formation of short voids, then long voids, and finally large voids with continuous compression.

Following the void development *in situ*, the fractal dimension (d) undergoes first a decrease at low strains and then an increase at large strains, suggesting that at large strains many micro-voids gather together to produce large voids, which is coincident with results using small-angle neutron scattering techniques to study the evolution of void morphology with pressed density of TATB (Mang & Hjelm, 2013). These large voids combine many micro-voids, which leads to a larger surface roughness and more irregular shapes at large scales and thus d slightly increases. From the behaviour of d , we can consider the existence of a critical point for the developing voids where many micro-voids gather together and transform into large ones.

The micro-voids existing in the original crystal are considered to be original defects. For soft X-ray nano-CT, domains with a density difference of about two times can be distinguished as they show good imaging contrast, while such a density contrast within one crystal is difficult to reach except for micro-voids. Thus, it is easier to distinguish voids than high-density zones in a crystal by X-ray nano-CT. In our experiments, the original micro-voids of the crystal were selected and followed in order to study their development. From our studies, we can speculate that higher-density zones could be defects in addition to small void groups, and act as the nucleation of voids, forming micro-voids and finally developing into large voids under compression, although it is difficult to distinguish the high-density zones by X-ray nano-CT.

4. Conclusion

Using the X-ray nano-CT technique, the structural evolution of micro-voids in TATB crystals under compression was studied *in situ*. The results indicate that the development of void groups mainly initiates from heterogeneously distributed

defects in the original crystal. These defects act as the nucleation for voids developing and produce stress concentration during compression, which further evolves into short and then long and large void groups. It is the growth of the void groups that leads to the final collapse of the TATB crystal. X-ray nano-CT has proven to be an efficient technique to capture *in situ* the evolution of voids under dynamic loading and helps to develop energetic and other functional materials with high performance.

Acknowledgements

Synchrotron beam times from National Synchrotron Radiation Lab (NSRL) and Beijing Synchrotron Radiation Facility (BSRF) are acknowledged.

Funding information

The following funding is acknowledged: National Natural Science Foundation of China (grant Nos. 51573177, 51890872, 51633009, 51790503).

References

- Balzer, J. E., Siviour, C. R., Walley, S. M., Proud, W. G. & Field, J. E. (2004). *Proc. R. Soc. London A*, **460**, 781–806.
- Barua, A., Horie, Y. & Zhou, M. (2012). *J. Appl. Phys.* **111**, 054902.
- Chen, L., Han, D., Bai, S. L., Zhao, F. & Chen, J. K. (2017). *Mech. Adv. Mater. Structures*, **24**, 737–744.
- Chen, L., Song, L. X., Li, J., Chen, P. Z., Huang, N. D. & Li, L. B. (2016). *Macromol. Mater. Eng.* **301**, 1390–1401.
- Chen, L., Zhou, W. M., Lu, J., Li, J., Zhang, W. H., Huang, N. D., Wu, L. & Li, L. (2015). *Macromolecules*, **48**, 7923–7928.
- Chen, P. W., Huang, F. L., Dai, K. D. & Ding, Y. S. (2005). *Int. J. Impact Eng.* **31**, 497–508.
- Chen, P. W., Huang, F. L. & Ding, Y. S. (2007). *J. Mater. Sci.* **42**, 5257–5280.
- Cheng, K. M., Liu, X. Y., Guan, D. B., Xu, T. & Wei, Z. (2007). *Prop. Explos. Pyrotech.* **32**, 301–306.
- Cheong, K. S., Stevens, K. J., Suzuki, Y., Uesugi, K. & Takeuchi, A. (2009). *Mater. Sci. Eng. A*, **513–514**, 222–227.
- Cui, J., Liu, D., Cai, Y., Pan, Z. J. & Zhou, Y. F. (2019). *Fuel*, **237**, 977–988.
- Dienes, J. K., Zuo, Q. H. & Kershner, J. D. (2006). *J. Mech. Phys. Solids*, **54**, 1237–1275.
- Furuta, S., Kobayashi, M., Uesugi, K., Takeuchi, A., Aoba, T. & Miura, H. (2018). *Materials*, **11**, 1308.
- Gallagher, H. G., Sherwood, J. N. & Vrcelj, R. M. (2014). *Chem. Cent. J.* **8**, 75.
- Garcea, S. C., Mavrogordato, M. N., Scott, A. E., Sinclair, I. & Spearing, S. M. (2014). *Compos. Sci. Technol.* **99**, 23–30.
- Garcea, S. C., Sinclair, I. & Spearing, S. M. (2015). *Compos. Sci. Technol.* **109**, 32–39.
- Jian, J., Yang, H., Zhao, X., Xuan, R., Zhang, Y., Li, D. & Hu, C. (2016). *J. Synchrotron Rad.* **23**, 600–605.
- Landron, C., Maire, E., Adrien, J., Suhonen, H., Cloetens, P. & Bouaziz, O. (2012). *Scr. Mater.* **66**, 1077–1080.
- Le Gros, M. A., McDermott, G., Cinquin, B. P., Smith, E. A., Do, M., Chao, W. L., Naulleau, P. P. & Larabell, C. A. (2014). *J. Synchrotron Rad.* **21**, 1370–1377.
- Mang, J. T. & Hjelm, R. P. (2013). *Propellants, Explosives, Pyrotech.* **38**, 831–840.
- Parab, N. D., Roberts, Z. A., Harr, M. H., Mares, J. O., Casey, A. D., Gunduz, I. E., Hudspeth, M., Claus, B., Sun, T., Fezzaa, K., Son, S. F. & Chen, W. W. (2016). *Appl. Phys. Lett.* **109**, 131903.
- Peterson, P. D., Mortensen, K. S., Idar, D. J., Asay, B. W. & Funk, D. J. (2001). *J. Mater. Sci.* **36**, 1395–1400.
- Rae, P. J., Goldrein, H. T., Palmer, S. J. P., Field, J. E. & Lewis, A. L. (2002). *Proc. R. Soc. London A*, **458**, 743–762.
- Ricard, J., Guigné, F. & Laiarinandrasana, L. (2014). *Engineering Fracture Mechanics*, **115**, 270–283.
- Shirai, R., Kunii, T., Yoneyama, A., Ooizumi, T., Maruyama, H., Lwin, T.-T., Hyodo, K. & Takeda, T. (2014). *J. Synchrotron Rad.* **21**, 795–800.
- Siviour, C. R., Laity, P. R., Proud, W. G., Field, J. E., Porter, D., Church, P. D., Gould, P. & Huntingdon-Thresher, W. (2008). *Proc. R. Soc. A*, **464**, 1229–1255.
- Sorrentino, A., Nicolás, J., Valcárcel, R., Chichón, F. J., Rosanes, M., Avila, J., Tkachuk, A., Irwin, J., Ferrer, S. & Pereiro, E. (2015). *J. Synchrotron Rad.* **22**, 1112–1117.
- Toda, H., Yamamoto, S., Kobayashi, M., Uesugi, K. & Zhang, H. (2008). *Acta Mater.* **56**, 6027–6039.
- Wu, S. C., Xiao, T. Q. & Withers, P. J. (2017). *Engineering Fracture Mechanics*, **182**, 127–156.
- Wu, Y. Q., Huang, F. L. & Zhang, Z. Y. (2012). *RSC Adv.* **2**, 4152–4163.
- Xue, C., Sun, J., Kang, B., Liu, Y., Liu, X. F., Song, G. B. & Xue, Q. B. (2010). *Propellants, Explosives, Pyrotech.* **35**, 333–338.
- Yeager, J. D., Luo, S. N., Jensen, B. J., Fezzaa, K., Montgomery, D. S. & Hooks, D. E. (2012). *Composites Part A*, **43**, 885–892.
- Yuan, Q., Zhang, K., Hong, Y., Huang, W., Gao, K., Wang, Z., Zhu, P., Gelb, J., Tkachuk, A., Hornberger, B., Feser, M., Yun, W. & Wu, Z. (2012). *J. Synchrotron Rad.* **19**, 1021–1028.
- Yuan, Z. N., Chen, H., Li, J. M., Dai, B. & Zhang, W. B. (2018). *Materials*, **11**, E732.
- Zhou, Z., Chen, P. W., Duan, Z. P. & Huang, F. L. (2012). *Strain*, **48**, 326–332.